

Atomic-scale insights into topotactic transformations in extra-large pore silicate zeolites using time-resolved 3D electron diffraction

Yi Luo^{1,4,5*}, Hao Xu^{2,3,5*}, Yue Han^{2,5}, Wen Tong², Meichen Jiao², Naihong Wang², Jingang Jiang², Xiaodong Zou^{1*}, Peng Wu^{2,3*}

¹Department of Materials and Environmental Chemistry, Stockholm University, Stockholm, Sweden.

²Shanghai Key Laboratory of Green Chemistry and Chemical Processes, State Key Laboratory of Petroleum Molecular & Process Engineering, School of Chemistry and Molecular Engineering, East China Normal University, Shanghai, China.

³Institute of Eco-Chongming, Shanghai, China.

⁴State Key Laboratory of Green Chemical Engineering and Industrial Catalysis, Sinopec Shanghai Research Institute of Petrochemical Technology, Shanghai, China.

⁵These authors contributed equally.

*Corresponding authors: Peng Wu (pwu@chem.ecnu.edu.cn), Xiaodong Zou (xzou@mmk.su.se), Hao Xu (hxu@chem.ecnu.edu.cn) and Yi Luo (luoy755.sshy@sinopec.com).

Summary

Understanding the atomic scale structural dynamics of phase transformations is crucial for developing new materials and tailoring the properties of the materials. However, many materials are obtained as polycrystalline powders with large unit cells and/or complex structures, making it challenging to investigate detailed structural changes using conventional X-ray diffraction techniques. Here, we employ time-resolved 3D electron diffraction (3D ED) to unravel the topotactic reactions and transformations of extra-large pore silicate zeolites ECNU-45 to ECNU-46. Notably, ECNU-45 features 3D interconnecting 24×10×10-ring channels, while ECNU-46 exhibits 1D 24-ring channels connected to 10-ring pockets. ECNU-45 and ECNU-46 are the first reported examples of pure silicate zeolites with pores larger than 22-rings. Our findings showcase detailed changes at six distinct tetrahedral Si sites, involving atom displacement, addition, and removal of framework atoms through bond breakage and formation. This work not only presents the discovery of novel zeolites but also provides unprecedented atomic-level insights into the dynamic processes of topotactic reactions. Our results have significant implications for advancing materials engineering and understanding complex solid-state reactions at an atomic scale.

Main text

Topotactic reactions play a pivotal role in the innovative engineering of various types of crystalline materials including zeolites, ceramics, alloys and battery cathodes (*1-18*). Conventional synthetic routes often encounter challenges in producing these materials, making topotactic reactions a key strategy for their preparations. While obtaining crystal structures of the starting and final phases is

1 crucial, unravelling the atomic-scale structural changes in reaction intermediates is equally important
2 for understanding the underlying mechanisms of these reactions (5, 10, 15, 19-24). This subtle
3 understanding is imperative for advancing the tailored design and synthesis of materials through
4 topotactic reactions.

5 A topotactic transformation involves the displacement or exchange of atoms within a crystal structure,
6 typically maintaining the overall framework of the original structure. It leads to products and
7 intermediates with similar unit cells and subtle structural differences. Furthermore, intermediate
8 structures often exhibit partially occupied and/or disordered atomic sites. While single-crystal X-ray
9 diffraction (SCXRD) has been powerful for determining atomic structures of large crystals ($>5\times5\times5$
10 μm^3) (10, 22-28), powder X-ray diffraction (PXRD) encounters challenges due to peak overlap (11,
11 14, 29, 30), hampering the detection of subtle structural changes during topotactic reactions.

12 In contrast, electrons interact with matter about 10^4 times more strongly than X-rays (31), making
13 them well-suited for studying crystals that are either too small for SCXRD or too complex for PXRD.
14 Although high-resolution electron microscopy has provided valuable insights into topotactic
15 transformations at atomic-scale (5, 8, 16, 20, 32-35), its application is often semi-quantitative and
16 limited to simple structures observable through 2D projections along specific directions. Over the
17 past two decades, three-dimensional electron diffraction (3D ED), sharing conceptual similarities
18 with SCXRD, has emerged as a powerful technique for structural studies, effectively overcoming
19 limitations associated with crystal size and complexity (36). Notably, 3D ED has become the most
20 important technique for structure determination of novel zeolites (36-38).

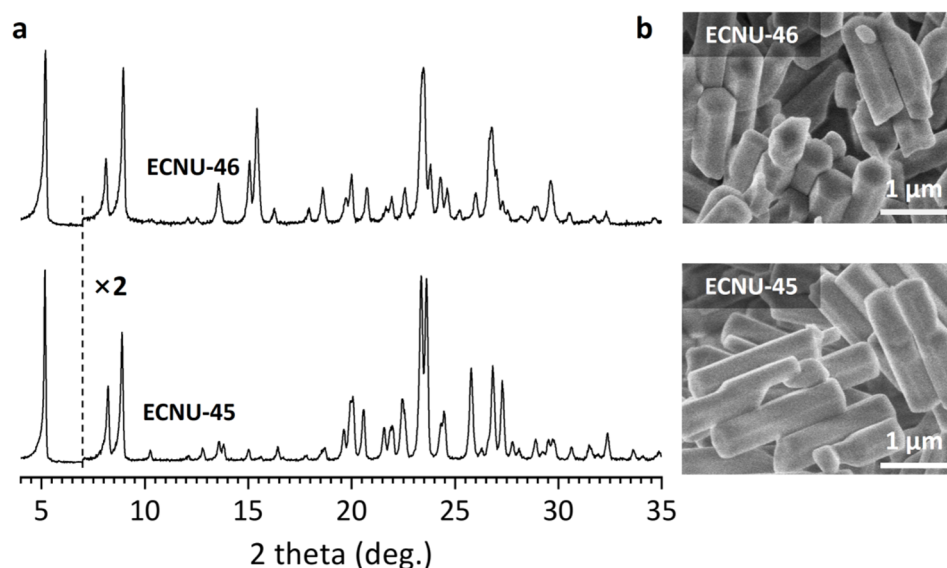
21 Zeolites are a class of microporous materials with well-defined pore structures and channel systems
22 in molecular dimensions. They are widely used as catalysts, adsorbents, and ion-exchangers. Most of
23 zeolites are synthesized as submicrometre- or nanometre-sized crystals and have complex framework
24 structures. The framework structures of zeolites are composed of TO_4 tetrahedra (T= Si, Al, B, Ge,
25 Ti, etc.). These tetrahedral atoms can be selectively removed from or incorporated into zeolite
26 framework structures through topotactic reactions. This distinctive structural characteristic makes
27 topotactic reactions a unique strategy for preparation of novel zeolites that are unfeasible through
28 conventional synthetic routes (11-14). One of them is the ADOR (assembly-disassembly-
29 organization-reassembly) strategy proposed by Čejka and Morris *et al.* that produced a series of new
30 zeolites (IPC-n series of zeolites) (11). By employing the heating or pressure induced topotactic
31 transformations, Corma *et al.* and Yu *et al.* have prepared novel zeolites ITQ-50 and ZEO-3 (4, 13),
32 respectively.

33 Despite extensive efforts to understand zeolite formation mechanisms, knowledge has primarily been
34 limited to the nanometre level (39-43). The direct visualization of atomic-scale structural
35 transformations during the topotactic reactions remains elusive, impeding a comprehensive
36 understanding of transformation mechanisms of zeolite topotactic reactions.

37 In this study, we present the synthesis of the two extra-large pore silicate zeolites, ECNU-45 and
38 ECNU-46, and their structure determinations using 3D ED. Both ECNU-45 and ECNU-46 contain

1 24-ring channels defined by 24 TO₄ tetrahedra (T = Si). They represent the first examples of pure
2 silica zeolites with pores \geq 24-ring. This is particularly noteworthy, as only three reported zeolites
3 ITQ-37 (30-ring, -ITV), ITQ-43 (28-ring, -IRT), and SYSU-3 (24-ring, -SYT) are known to have
4 pores \geq 24-rings, and all of them are Ge-rich silicogermanates, thermally and hydrothermally
5 unstable (44-46). ECNU-46 was derived from ECNU-45 by topotactic transformation. While ECNU-
6 45 features a 3D 24 \times 10 \times 10-ring channel system, ECNU-46 exhibits a 1D 24-ring channel
7 connected to 10-ring pockets. Importantly, we demonstrate for the first time that time-resolved 3D
8 ED can capture topotactic structural transformations at the atomic scale, from the starting phase,
9 through various reaction intermediates at distinct time points, to the final product. These detailed
10 structure evolutions throughout the entire topotactic reaction provide new insights into the atomic-
11 scale mechanisms governing the zeolite transformations.

12 ECNU-45 was hydrothermally synthesized using 1,1,6,6-tetramethyl-1,6-diazacyclododecane-1,6-
13 diium hydroxide as the organic structure-directing agent (OSDA; Fig. 1 and Supplementary Fig. 1;
14 see Supplementary materials), and used as the starting phase. The final product ECNU-46 was
15 prepared via topotactic reactions of ECNU-45 in an acidic solution of HCl/EtOH/H₂O (1 M) at 190 °C
16 for 24 h (Fig. 1). While the framework of ECNU-46 was stable after calcination at 550 °C in air, that
17 of ECNU-45 collapsed after calcination where all OSDAs were removed (Supplementary Fig. 2).



18

19 **Fig. 1 PXR D patterns (a) and scanning electron microscopy (SEM) images (b) of silicate zeolites ECNU-**
20 **45 and ECNU-46.** The PXR D intensity profiles (Cu K α) above 7° are scaled two times to show more details.
21 SEM images show that the crystals of ECNU-45 and ECNU-46 both have a hexagonal morphology.

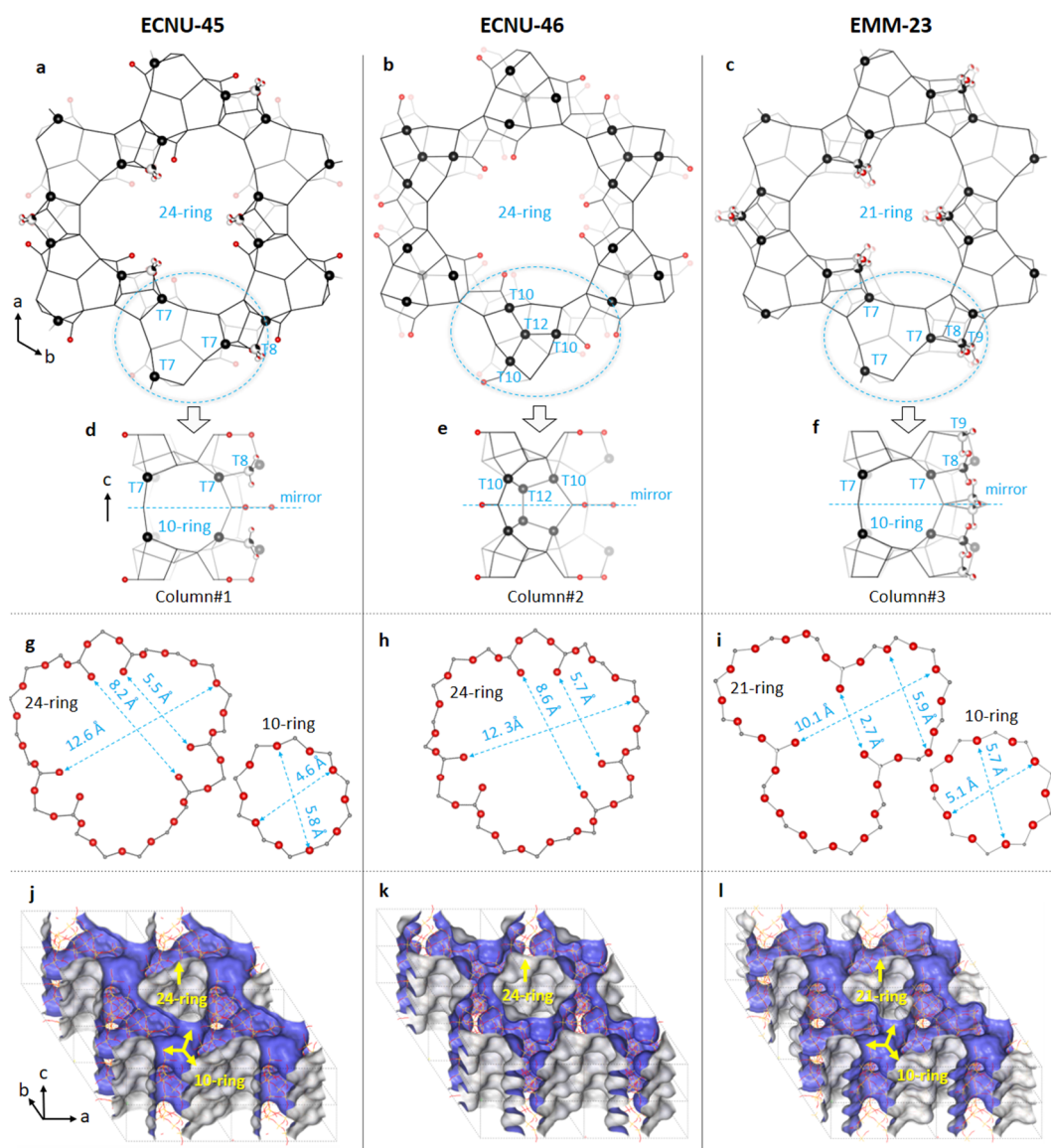
22 *Structure determination of ECNU-45 and ECNU-46*

23 Because of the small crystal size of ECNU-45 and ECNU-46, 3D ED was applied to determine their
24 crystal structures. Both structures have similar unit cell and the same space group *P*-62c
25 (Supplementary Fig. 3). The unit cell parameters were further refined by Pawley fit from the PXR D
26 data to be $a = 19.9616$ and $c = 13.8771$ Å for ECNU-45 and $a = 19.7848$ and $c = 14.1435$ Å for

1 ECNU-46 (Supplementary Fig. 4). While the low angle PXRD profiles are similar for ECNU-45 and
2 ECNU-46, the high angle ($2\theta > 15^\circ$) peak intensities are considerably different (Fig. 1). This indicates
3 that their framework structures are different despite the same space group and similar unit cells. The
4 unit cell parameters of ECNU-45 and ECNU-46 are also similar to those of zeolite EMM-23 ($a =$
5 19.7480 and $c = 13.8585$ Å, framework type: **-EWT**) (47), which has a different space group $P31c$.

6 The structures of ECNU-45 and ECNU-46 were solved and refined using 3D ED data, which were
7 found to be highly related but distinct in topology (Fig. 2, Supplementary Fig. 5, and Supplementary
8 Table 1). While ECNU-45 has a 3D intersecting channel system defined by $24 \times 10 \times 10$ -rings (Figs.
9 2a and j), ECNU-46 has a 1D 24-ring channel system connected to 10-ring pockets (Figs. 2b and k).
10 The frameworks of both ECNU-45 and ECNU-46 are constructed by columnar building units along
11 the c -axis, as indicated in Figs. 2d and e. Each 24-ring channel is built from six such columns, and
12 each column is associated to three 24-ring channels (Supplementary Figs. 6a and b). The column (#1)
13 in ECNU-45 contains 10-ring pores (Fig. 2d and Supplementary Fig. 6c), which connect the 24-ring
14 channels to form a 3D interconnected $24 \times 10 \times 10$ -ring channel system. Both ECNU-45 and ECNU-
15 46 have eight symmetry-independent TO_4 tetrahedral sites; six of them (T1 to T6) have similar
16 connectivity and positions (differ by < 0.40 Å for T1-T5 and 0.68 Å for T6). The remaining two sites
17 (denoted T7 and T8 in ECNU-45 and T10 and T12 in ECNU-46) are different (Figs. 2a and b;
18 Supplementary Figs. 6a and b; Supplementary cif files). Although their positions are very different
19 (differ by 1.42 Å), T7 in ECNU-45 and T10 in ECNU-46 share the same connectivity to three T sites
20 (T3, T5, T6) (Figs. 2a and b; Supplementary cif files). However, the fourth connectivity is different;
21 T7 is connected to T8, while T10 is connected to T12. T8 is partially occupied with a very low
22 occupancy (0.27) and connects to two T7, while T12 is fully occupied and connects to three T7 and
23 one T12 (columns #1 and #2 in Fig. 2; Supplementary Figs. 6c and d). The new T10-T12 and T12-
24 T12 connections block the 10-ring channels and result in a 1D 24-ring channel system in ECNU-46.

25 The framework of ECNU-45 is also similar to that of EMM-23 (47), both have 3D intersecting
26 channels, defined by $24 \times 10 \times 10$ -rings and $21 \times 10 \times 10$ -rings (Figs. 2a and c), respectively. All T-
27 sites (T1 to T8) in ECNU-45 also exist in EMM-23 (column#3, Figs. 2d and f). The difference is that
28 EMM-23 has a higher occupancy (0.67) occupancy at the T8 site than ECNU-45 (0.27). In addition,
29 EMM-23 has an additional T site (T9, occupancy 0.33) (Fig. 2f) (47). The refined framework
30 composition per unit cell is $[\text{Si}_{160}\text{O}_{109}(\text{OH})_{22}]$ for ECNU-45 and $[\text{Si}_{162}\text{O}_{118}(\text{OH})_{12}]$ for ECNU-46,
31 compared to $[\text{Si}_{164}\text{O}_{116}(\text{OH})_{24}]$ for EMM-23 reported early (47). The free diameters of the 24-rings in
32 ECNU-45 and ECNU-46 are very similar, 12.6×8.2 Å and 12.3×8.6 Å, respectively (Figs. 2g and
33 h). In comparison, the 21-ring pore opening in EMM-23 is much smaller (10.1×2.7 Å), which has a
34 trilobe-shape resembling three fused 10-ring channels (Fig. 2i). The free diameters of 10-ring
35 channels in ECNU-45 and EMM-23 are similar, 5.8×4.6 Å and 5.7×5.1 Å, respectively.



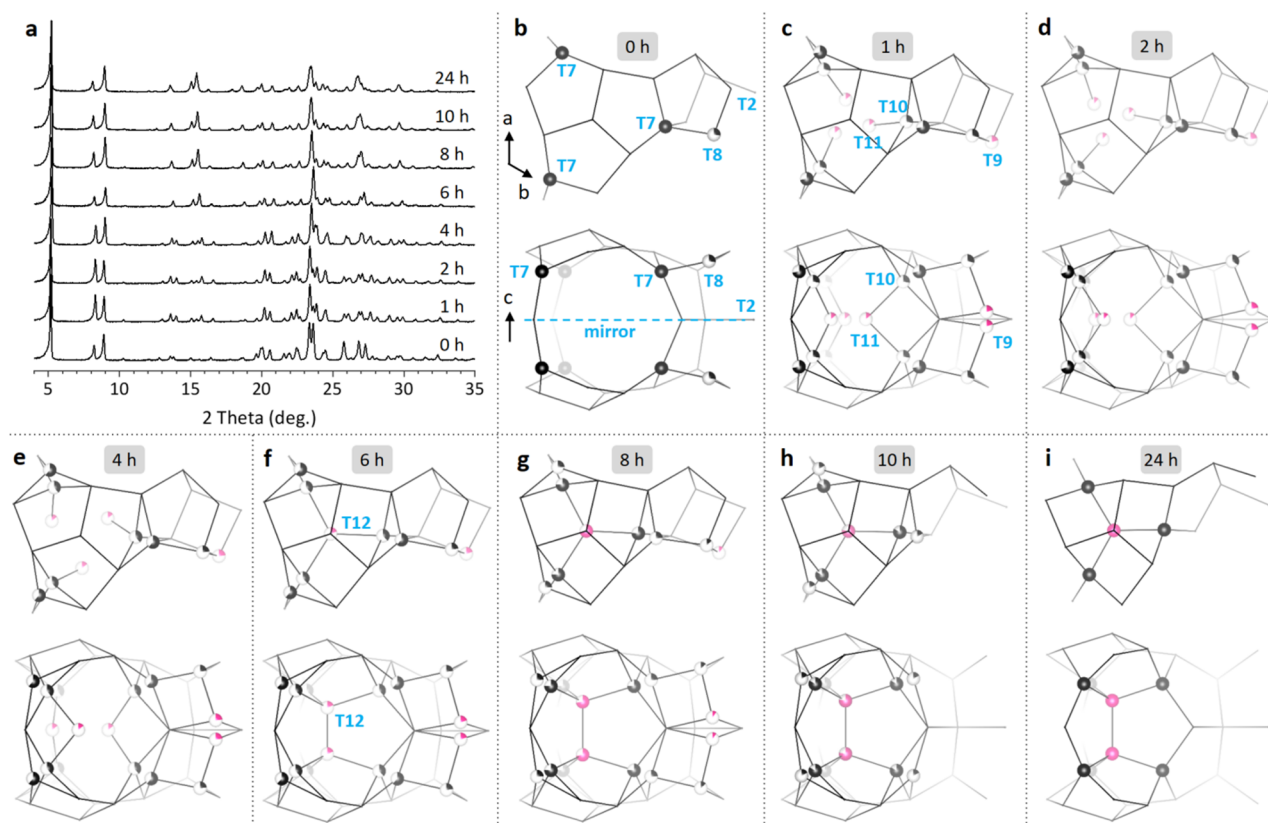
1
2 **Fig. 2 Comparison of the framework structure, pore size and channel system of ECNU-45, ECNU-46**
3 **and EMM-23. (a-c)** The framework structure showing the extra-large channels with the columnar building
4 unit marked by rings. **(d-f)** The columnar building unit viewed perpendicular to the column. Only the T-T
5 connections and terminal oxygen atoms (in red) are shown for clarity. The T-sites that differ mostly are
6 highlighted with black balls. Fan-shaped balls represent partially occupied sites and the white areas correspond
7 to vacancies. **(g-i)** The pore openings and free diameters after subtracting the oxygen diameter of 2.70 Å. **(j-l)**
8 The channel system showing connections of the channels. **(a, d, g, j)** ECNU-45: the refined occupancy is 100%
9 for T7 and 27% for T8, see column #1. Because of the low occupancy (0.27) at T8, the extra-large channel of
10 ECNU-45 is mainly defined by 24-rings (on average > 23-rings). The 24-ring channel is interconnected by the
11 10-ring channels, resulting in a 3D 24 × 10 × 10-ring channel system. **(b, e, h, k)** ECNU-46: all T-sites are
12 fully occupied. T10 corresponds to T7 in ECNU-45 but moved by 1.42 Å and connected to T12, which blocks
13 the 10-ring channels in ECNU-45 (column #2) and turn them into 10-ring pockets. This results in a 1D 24-ring
14 channel system. **c, EMM-23:** the refined occupancy is 100% for T7, 67% for T8 and 33% for T9, see column
15 #3. The 21-ring channels are interconnected with perpendicular 10-ring channels, forming a 3D 21 × 10 × 10-
16 ring channel system. The pore sizes and envelope of ECNU-45 were calculated based on the framework
17 structure without the (T8)O₄ tetrahedra. There are three terminal T atoms (T2, T6 and T7/T8) in ECNU-45,
18 and two terminal T atoms (T2 and T6) in ECNU-46.

1 *Structure evolution by time-resolved 3D ED and insights into the reaction mechanism*

2 The topotactic transformation from a 3D $24 \times 10 \times 10$ -ring channel system in ECNU-45 to a 1D 24-
3 ring channel system in ECNU-46 involves displacement, addition and removal of framework atoms,
4 bond formation and bond breakage in the framework. It is therefore important to follow the structure
5 evolution at atomic scale throughout the entire topotactic transformations to understand the reaction
6 mechanism. To achieve this, we investigated the reaction intermediates prepared in an acidic medium
7 (HCl/EtOH/H₂O, 1 M) at 190 °C at different treatment time points, namely 0, 1, 2, 4, 6, 8, 10, and 24
8 h by combining SEM, PXRD, solid-state ²⁹Si MAS NMR and thermogravimetric analysis (TGA).
9 More importantly, we applied time-resolved 3D ED to follow the detailed structural changes at atomic
10 scale.

11 SEM shows the crystal sizes and morphology remained the same during the topotactic reaction
12 (Supplementary Fig. 7). PXRD indicates considerable structural changes of the reaction intermediates,
13 as shown by the changes of the peak positions and intensities (Fig. 3a; Supplementary Fig. 8a).
14 Pawley fitting of the PXRD patterns shows some minor contraction (0-4 h) followed by expansion
15 (4-8 h) of the unit cell volume (Supplementary Fig. 9). In order to gain a deeper insight into the
16 topotactic reactions and transformations, we further collected 3D ED data on the reaction product
17 obtained at each time point and determined the 3D atomic structure of the intermediate (Fig. 3b-i;
18 Supplementary Table 1). The high 3D ED data quality allowed us to locate partially occupied atomic
19 sites from the difference Fourier maps and determine their occupancies. The refinements converged
20 to reasonable *R*₁-values from 0.1226 to 0.1732 for $F^2 > 2.0\sigma(F^2)$, and Si-O bond distances (1.55 to
21 1.66 Å, on average 1.59 Å) and O-Si-O angles (102.7 to 117.0°, on average 109.5°) (Supplementary
22 Table 1).

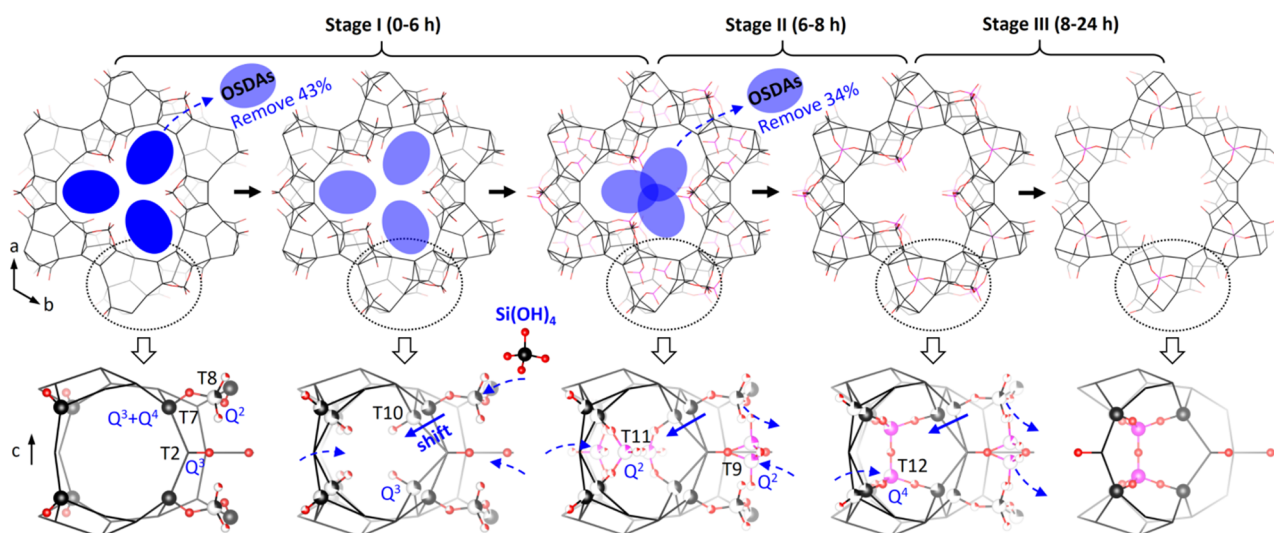
23 We compared the atomic structures of the starting material (0 h), reaction intermediates (1-10 h) and
24 the final product (24 h), which provided several new insights of topotactic reactions (Figs. 3b-I;
25 Supplementary videos 1 and 2). We found the reactions involved six topologically independent sites
26 (T7-T12, Fig. 3 and Supplementary Fig. 10). All these T sites are two- or three-connected (Q² and
27 Q³) and their occupancies changed throughout the reactions. The major changes include shift of Q³
28 species from T7 to T10, addition of new framework atoms at T9 and T11, shift of Q² species from
29 T11 to T12, and finally removal of Q² species at T8 and T9. Consequently, a number of new bonds
30 were formed (in **bold**, T2-O-T9, T6-O-T9, T8-O-T9, T10-O-T11, T10-O-T12). The Si species at T9
31 and T11 had very low occupancies (< 23%) and were only observed in the intermediate structures (1-
32 8 h). Except for T10-O-T12, all other new bonds broke and the Si species at T8 and T9 completely
33 dissolved in the later stages of the reactions (6-10 h). The resulting framework ECNU-46 has only
34 two Q³ species (at T3 and T6) compared to that of ECNU-45, which has three Q³ species (at T3, T6
35 and T7).



1

2 **Fig. 3 Topotactic reaction intermediates studies using 3D ED.** a, Experimental PXRD patterns (CuK α) of
 3 intermediates obtained at reaction times of 0, 1, 2, 4, 6, 8, 10 and 24 h. b-i, Intermediate structures at 0, 1, 2,
 4, 6, 8, 10 and 24 h (only present part of the columns). The reactions were observed to have taken place at T8,
 5 T9, T10, T11 and T12. Q³ species at T7 were gradually displaced to T10 and subsequently reacted with Si(OH)₄
 6 species to form T11 (Q² species, 0-4 h). Q² species at T11 were all transferred to T12 during 4 to 6 h. The
 7 successive displacement of Q³ species at T7 to T10 and the intercalation of Si(OH)₄ species at T12 blocked
 8 the 10-ring channels and resulted in the framework structure of ECNU-46. T sites presented with balls are
 9 those involved in the topotactic reactions and transformations. The black ones are derived from the framework
 10 structure of ECNU-45, while the pink ones are new T sites formed via reactions between the framework Si-
 11 OH terminals and Si(OH)₄ species. Those T sites with fan-shapes are partially occupied, and the white areas
 12 correspond to vacancies. O atoms are omitted for clarity.

13 Notably, the OSDAs located in the pores of ECNU-45 were removed during the topotactic reactions.
 14 TGA revealed a stepwise removal of the OSDAs (Supplementary Fig. 9a), 43% during 0 - 1 h, 11%
 15 during 1 - 4 h, followed by the complete removal (34%) of the OSDAs during 4 - 6 h. Although it
 16 was challenging to obtain atomic positions of the OSDAs from the 3D ED data, the locations of the
 17 molecules could be identified from the difference Fourier maps of the reaction intermediates
 18 (Supplementary Fig. 12). We found that the OSDAs were initially located at the intersections of the
 19 10-ring and 24-ring channels (0 h). They remained at the same locations despite 43 % of the OSDAs
 20 being removed (1 h). Most of the remaining OSDAs migrated to the center of the extra-large channels
 21 (2 - 4 h). No strong extra peaks were observed in the difference Fourier map of the reaction
 22 intermediate at 6 h, indicating the absence of the OSDAs. The results obtained from 3D ED data agree
 23 with the TGA results and also with the modelling of the OSDA positions (Supplementary Fig. 13).



1

2 **Fig. 4 Topotactic reaction and transformation mechanisms.** The topotactic reaction and transformation
 3 process can be divided into three stages. In the first stage, about half of the OSDAs were firstly and rapidly
 4 removed from the channels and the Q^3 species at T7 partially shifted to T10. The Q^3 species at T2, T7 and T10
 5 were then reacted with $Si(OH)_4$ species and formed the Q^2 species at T9 and T11. Meanwhile, most of the
 6 remaining OSDAs were migrated to the center of the extra-large channels. In the second stage, the remaining
 7 OSDAs were almost all removed; more Q^3 species at T7 shifted to T10, and the Q^2 species at T11 shifted to
 8 T12 and became Q^4 species. In the third stage, the remaining Q^3 species at T7 kept shifting to T10 and reacting
 9 with $Si(OH)_4$ species until the T10 and T12 became fully occupied. The Q^2 species at T8 and T9 were gradually
 10 removed in the end. T sites in black balls are the original ones of ECNU-45 that were involved in the reaction,
 11 and T sites in pink balls are the additional ones formed during the reaction. The blue-dotted arrows toward and
 12 away from the T sites show the addition and removal of $Si(OH)_4$ species, respectively. Atoms with fan-shapes
 13 are partially occupied, and the white areas correspond to vacancies. The terminal O atoms are in red. The other
 14 atoms are not shown for clarity. The $Si(OH)_4$ species were leached from the crystals (Supplementary Table 2).

15

16 The structural information of the intermediates obtained from the 3D ED data enables new insights
 17 into reaction mechanisms of the topotactic transformation from ECNU-45 to ECNU-46 under the
 18 acidic treatment (Fig. 4). We anticipate the interplay between the stepwise removal of the OSDAs,
 19 the incorporation of new framework species and subsequent removal of those species played a pivotal
 20 role and ensured the framework stability throughout the topotactic reactions. Acid treatment
 21 expeditiously eliminates approximately half of the OSDAs from the channels, which facilitates the
 22 shift of some Q^3 species from T7 to T10 and subsequently incorporation of additional framework
 23 species at T9 and T11 to bind and stabilize the T7 and T10 sites, respectively. Meanwhile, the
 24 remaining OSDAs predominantly migrate towards the center of the extra-large channels, in proximity
 25 to the Q^2 species at T8 and T9, thus maintaining good structural stability for the later topotactic
 26 reaction. The migration of OSDAs would also facilitate the shift of more Q^3 species from T7 to T10,
 27 allowing the shift of Q^2 species at T11 to T12 to form Q^4 species (Supplementary Fig. 10a). This
 28 increases the stability of the framework, allowing for further removal of the OSDAs. After the
 29 complete removal of the OSDAs (6 h), most Q^3 species at T7 shifted to T10 and reacted with $Si(OH)_4$

1 species at T12 until both T10 and T12 were fully occupied. The unstable Q² species at T8 and T9
2 were gradually dissolved. These sequential events led to the transformation of ECNU-45 into ECNU-
3 46 through topotactic reactions. This is in contrast to direct calcination where the framework of
4 ECNU-45 collapsed upon the removal of the OSDAs (Supplementary Fig. 2).

5 To our knowledge, it is the first time that time-resolved 3D ED has been applied to the study of a
6 highly complex topotactic transformation at the atomic scale. It enabled the visualization of detailed
7 structural changes including atom displacement, addition, and removal, as well as bond forming and
8 bond breaking. It also discovered the interplay between the framework atoms and OSDAs, which
9 provides new insights into the formation mechanism of a zeolite and represents significant
10 advancements in zeolite chemistry. We believe time-resolved 3D ED not only opens a new avenue
11 for studying topotactic transformations in diverse crystalline materials at the atomic scale but also
12 holds immersing potential for accelerating the development of novel functional materials.

13 Reference

- 14 1. X. Jia, C. Liu, Z. G. Neale, J. Yang, G. Cao, Active Materials for Aqueous Zinc Ion Batteries:
15 Synthesis, Crystal Structure, Morphology, and Electrochemistry. *Chem. Rev.* **120**, 7795–7866
16 (2020).
- 17 2. L. De Trizio, L. Manna, Forging Colloidal Nanostructures via Cation Exchange Reactions.
18 *Chem. Rev.* **116**, 10852–10887 (2016).
- 19 3. A. Kumar *et al.*, Solid-State Reaction Synthesis of Nanoscale Materials: Strategies and
20 Applications. *Chem. Rev.* **122**, 12748–12863 (2022).
- 21 4. J. Li *et al.*, A 3D extra-large-pore zeolite enabled by 1D-to-3D topotactic condensation of a
22 chain silicate. *Science* **379**, 283–287 (2023).
- 23 5. Z. Li, M. Saruyama, T. Asaka, Y. Tatetsu, T. Teranishi, Determinants of crystal structure
24 transformation of ionic nanocrystals in cation exchange reactions. *Science* **373**, 332–337 (2021).
- 25 6. A. P. Amrute, Z. Łodziana, H. Schreyer, C. Weidenthaler, F. Schüth, High-surface-area
26 corundum by mechanochemically induced phase transformation of boehmite. *Science* **366**, 485–
27 489 (2019).
- 28 7. D. Lei, J. Benson, A. Magasinski, G. Berdichevsky, G. Yushin, Transformation of bulk alloys
29 to oxide nanowires. *Science* **355**, 267–271 (2017).
- 30 8. R. A. House *et al.*, Superstructure control of first-cycle voltage hysteresis in oxygen-redox
31 cathodes. *Nature* **577**, 502–508 (2020).
- 32 9. W. Zhang *et al.*, Reconstructed covalent organic frameworks. *Nature* **604**, 72–79 (2022).
- 33 10. M. I. Gonzalez *et al.*, Confinement of atomically defined metal halide sheets in a metal–organic
34 framework. *Nature* **577**, 64–68 (2020).
- 35 11. S. A. Morris *et al.*, In situ solid-state NMR and XRD studies of the ADOR process and the
36 unusual structure of zeolite IPC-6. *Nat. Chem.* **9**, 1012–1018 (2017).
- 37 12. W. J. Roth, P. Nachtigall, R. E. Morris, J. Čejka, Two-Dimensional Zeolites: Current Status and
38 Perspectives. *Chem. Rev.* **114**, 4807–4837 (2014).
- 39 13. J. L. Jordá *et al.*, Synthesis of a Novel Zeolite through a Pressure-Induced Reconstructive Phase
40 Transition Process. *Angew. Chem. Int. Ed.* **52**, 10458–10462 (2013).

- 1 14. E. Verheyen *et al.*, Design of zeolite by inverse sigma transformation. *Nat. Mater.* **11**, 1059–
2 1064 (2012).
- 3 15. X. Zhou *et al.*, Discovery of chalcogenides structures and compositions using mixed fluxes.
4 *Nature*, 1–6 (2022).
- 5 16. R. J. Macfarlane, M. R. Jones, B. Lee, E. Auyeung, C. A. Mirkin, Topotactic Interconversion of
6 Nanoparticle Superlattices. *Science* **341**, 1222–1225 (2013).
- 7 17. J. V. Badding, High-Pressure Synthesis, Characterization, and Tuning of Solid State Materials.
8 *Annu. Rev. Mater. Sci.* **28**, 631–658 (1998).
- 9 18. S. J. Lyle, T. M. Osborn Popp, P. J. Waller, X. Pei, J. A. Reimer, O. M. Yaghi, Multistep Solid-
10 State Organic Synthesis of Carbamate-Linked Covalent Organic Frameworks. *J. Am. Chem. Soc.*
11 **141**, 11253–11258 (2019).
- 12 19. X. Hua *et al.*, Revisiting metal fluorides as lithium-ion battery cathodes. *Nat. Mater.* **20**, 841–
13 850 (2021).
- 14 20. A. W. Xiao *et al.*, Understanding the conversion mechanism and performance of monodisperse
15 FeF₂ nanocrystal cathodes. *Nat. Mater.* **19**, 644–654 (2020).
- 16 21. H. Liu *et al.*, Capturing metastable structures during high-rate cycling of LiFePO₄ nanoparticle
17 electrodes. *Science* **344**, 1252817 (2014).
- 18 22. W. Meng *et al.*, An elastic metal–organic crystal with a densely catenated backbone. *Nature* **598**,
19 298–303 (2021).
- 20 23. S.-Y. Zhang *et al.*, Synthesis of a Chiral Crystal Form of MOF-5, CMOF-5, by Chiral Induction.
21 *J. Am. Chem. Soc.* **137**, 15406–15409 (2015).
- 22 24. Y. Ohki *et al.*, Nitrogen reduction by the Fe sites of synthetic [Mo₃S₄Fe] cubes. *Nature* **607**, 86–
23 90 (2022).
- 24 25. Z. Huang, P. S. White, M. Brookhart, Ligand exchanges and selective catalytic hydrogenation
25 in molecular single crystals. *Nature* **465**, 598–601 (2010).
- 26 26. J. Hicks, P. Vasko, J. M. Goicoechea, S. Aldridge, Synthesis, structure and reaction chemistry
27 of a nucleophilic alumanyl anion. *Nature* **557**, 92–95 (2018).
- 28 27. S. D. Pike, A. L. Thompson, A. G. Algarra, D. C. Apperley, S. A. Macgregor, A. S. Weller,
29 Synthesis and Characterization of a Rhodium(I) σ -Alkane Complex in the Solid State. *Science*
30 **337**, 1648–1651 (2012).
- 31 28. Y. Wang, S. Liu, H. Yang, H. Li, Y. Lan, Q. Liu, Structure, reactivity and catalytic properties
32 of manganese-hydride amidate complexes. *Nat. Chem.* **14**, 1233–1241 (2022).
- 33 29. F. Lin *et al.*, Synchrotron X-ray Analytical Techniques for Studying Materials Electrochemistry
34 in Rechargeable Batteries. *Chem. Rev.* **117**, 13123–13186 (2017).
- 35 30. F. Gramm *et al.*, Complex zeolite structure solved by combining powder diffraction and electron
36 microscopy. *Nature* **444**, 79–81 (2006).
- 37 31. D. N. Wang, W. Kühlbrandt, Three-dimensional electron diffraction of plant light-harvesting
38 complex. *Biophys. J.* **61**, 287–297 (1992).
- 39 32. T. Meiners, T. Frolov, R. E. Rudd, G. Dehm, C. H. Liebscher, Observations of grain-boundary
40 phase transformations in an elemental metal. *Nature* **579**, 375–378 (2020).
- 41 33. J. Bae *et al.*, Phase Transformation Behavior of a Two-Dimensional Zeolite. *Angew. Chem. Int.*
42 *Ed.* **58**, 10230–10235 (2019).

- 1 34. M. H. Oh *et al.*, Galvanic Replacement Reactions in Metal Oxide Nanocrystals. *Science* **340**,
2 964–968 (2013).
- 3 35. S. Van Aert, K. J. Batenburg, M. D. Rossell, R. Erni, G. Van Tendeloo, Three-dimensional
4 atomic imaging of crystalline nanoparticles. *Nature* **470**, 374–377 (2011).
- 5 36. M. Gemmi *et al.*, 3D Electron Diffraction: The Nanocrystallography Revolution. *ACS Cent. Sci.*
6 **5**, 1315–1329 (2019).
- 7 37. Z. Huang, T. Willhammar, X. Zou, Three-dimensional electron diffraction for porous crystalline
8 materials: structural determination and beyond. *Chem. Sci.* **12**, 1206–1219 (2021).
- 9 38. Y. Luo, B. Wang, S. Smeets, J. Sun, W. Yang, X. Zou, High-throughput phase elucidation of
10 polycrystalline materials using serial rotation electron diffraction. *Nat. Chem.* **15**, 483–490
11 (2023).
- 12 39. A. I. Lupulescu, J. D. Rimer, In Situ Imaging of Silicalite-1 Surface Growth Reveals the
13 Mechanism of Crystallization. *Science* **344**, 729–732 (2014).
- 14 40. S. Mintova, N. H. Olson, V. Valtchev, T. Bein, Mechanism of Zeolite A Nanocrystal Growth
15 from Colloids at Room Temperature. *Science* **283**, 958–960 (1999).
- 16 41. C. S. Cundy, P. A. Cox, The hydrothermal synthesis of zeolites: Precursors, intermediates and
17 reaction mechanism. *Micropor. Mesopor. Mater.* **82**, 1–78 (2005).
- 18 42. C. Paula *et al.*, Phase Transformations in Porous Materials Studied by In Situ Solid-State NMR
19 Spectroscopy and In Situ X-ray Diffraction. *J. Phys. Chem. C* **124**, 19136–19145 (2020).
- 20 43. J. Shin, N. H. Ahn, M. A. Cambor, S. J. Cho, S. B. Hong, Intraframework Migration of
21 Tetrahedral Atoms in a Zeolite. *Angew. Chem. Int. Ed.* **53**, 8949–8952 (2014).
- 22 44. J. Sun *et al.*, The ITQ-37 mesoporous chiral zeolite. *Nature* **458**, 1154–1157 (2009).
- 23 45. J. Jiang *et al.*, Synthesis and Structure Determination of the Hierarchical Meso-Microporous
24 Zeolite ITQ-43. *Science* **333**, 1131–1134 (2011).
- 25 46. C. Zhang *et al.*, An Extra-Large-Pore Zeolite with 24×8×8-Ring Channels Using a Structure-
26 Directing Agent Derived from Traditional Chinese Medicine, *Angew. Chem. Int. Ed.* **57**, 6486–
27 6490 (2018).
- 28 47. T. Willhammar *et al.*, EMM-23: A Stable High-Silica Multidimensional Zeolite with Extra-
29 Large Trilobe-Shaped Channels. *J. Am. Chem. Soc.* **136**, 13570–13573 (2014).

30

31 **Data availability**

32 All the data that support the findings of this study are available in this paper and its Supplementary
33 Information. A preprint of this work has been deposited in ChemRxiv, [DOI: 10.26434/chemrxiv-](https://doi.org/10.26434/chemrxiv-2023-pdtg4)
34 [2023-pdtg4](https://doi.org/10.26434/chemrxiv-2023-pdtg4).

35 **Acknowledgements**

36 The authors acknowledge Dr. Wende Hu for the help of molecular simulation. The authors
37 acknowledge financial support from the National Natural Science Foundation of China (22222201
38 and 21972044), the National Key R&D Program of China (2021YFA1501401), the Swedish Research
39 Council (VR, 2019-00815), and the Knut and Alice Wallenberg Foundation (KAW, 2018.0237). The

1 structure determination by 3D ED was performed at the Electron Microscopy Center (EMC) at
2 Stockholm University through ARTEMI. The authors also acknowledge KAW for an equipment grant
3 for the electron microscopy facilities at the EMC, Stockholm University.

4 **Author contributions**

5 P. W and H. X. directed the design and preparation of zeolite materials. X. Z. and Y. L. directed the
6 topotactic reaction and structural studies using 3D ED. Y. L. conceived the idea of topotactic reaction
7 studies using 3D ED, and performed the 3D ED experiments and structural studies. Y. H., W. T., M.
8 J. and N. W. synthesized all the zeolite materials and performed the general characterizations (PXRD,
9 SEM, ICP, BET, TGA, etc.). J. J. performed the NMR experiments. Y. L., H. X., Y. H. and X. Z.
10 interpreted the results and wrote the manuscript. All authors reviewed and commented on the
11 manuscript.

12 **Competing interests**

13 The authors declare no competing interests.